RSC Advances

ROYAL SOCIETY OF CHEMISTRY

PAPER

View Article Online
View Journal | View Issue

Check for updates

Cite this: *RSC Adv.*, 2021, **11**, 25266

Fast conversion of lithium (poly)sulfides in lithium–sulfur batteries using three-dimensional porous carbon†

Xinghua Liang,*[a] Xi Wu,[a] Shuaibo Zeng,*[b] Wei Xu,[b] Xingtao Jiang[a] and Lingxiao Lan[a]

The slow redox kinetics of polysulfide hinders the rapid and complete conversion between soluble polysulfides and Li_2S_2/Li_2S, resulting in unsatisfactory rate and cycle performance in lithium-sulfur batteries. Electrochemical catalysis, one effective method, promotes the reaction kinetics and inhibits the "shuttle effect". Here, we present a three-dimensional ordered macro-porous carbon with abundant cobalt–nitrogen–carbon active sites as a matrix catalyst, leading to accelerated polysulfide redox kinetics. In addition, the interconnected conductive frameworks with ordered macro-porous carbon afford fast ion/electron transport and provide sufficient space to adapt to the volume expansion of the sulfur electrode. Owing to the aforementioned advantages, a lithium–sulfur battery with the matrix catalyst delivers a high specific capacity (1140 mA h g^{-1} at 0.1C) and a low capacity decay rate (0.0937% per cycle over 500 cycles). Moreover, there is a high rate capacity (349.1 mA h g^{-1}) even at the high current density of 2C and sulfur loading of 3.8 mg cm^{-2} due to the improved polysulfide redox kinetics by a catalytic effect.

Received 7th April 2021
Accepted 29th June 2021

DOI: 10.1039/d1ra02704b

rsc.li/rsc-advances

Introduction

With the increasing importance of new-energy vehicles powered by lithium-ion batteries, governments all over the world have formulated a timetable for banning the sale of petrol cars to promote the electrification of vehicles.[1–3] Within a few short years, various supporting policies were announced to encourage the new-energy automobile industry. However, the actual capacities of automobile power batteries are close to the theoretical capacity of the battery materials, and they still cannot meet the long-cruising demand of electric vehicles.[4] Car owners must stop to recharge the batteries during distance driving. The long recharge time and capacity attenuation after multiple charging will thus be an issue. Furthermore, it is difficult for the original battery material system to make a big breakthrough in energy density.[5,6] Therefore, new material systems must be developed to meet the ever-changing demands of the new-energy vehicle market.

Over the history of the lithium-ion battery, scientists have successively developed a variety of positive, negative, and electrolyte materials.[7–11] Compared with the current traditional lithium-ion battery anode materials, sulfur, a geographically ubiquitous element with high theoretical specific capacity (1672 mA h g^{-1}), is regarded as one of the most promising cathode materials for lithium-ion batteries.[12–14] However, it still suffers from fatal flaws that delay the pace of engineering application, such as the insulative properties of sulfur and low-order lithium sulfide (Li_2S_2, Li_2S),[15,16] solubility of high-order lithium sulfide (Li_2S_8, Li_2S_6, Li_2S_4),[17,18] volumetric expansibility during discharge,[19,20] and low areal sulfur loading.[21,22] These features lead to poor cyclic stability and rate performance.

Many approaches have been proposed to solve the above-mentioned problems. Various carbon skeletons have been deployed to hold up sulfur by constructing sulfur–carbon composite materials.[23] However, the rate performance of Li–S batteries employed with sulfur/carbon cathode showed no significant improvement due to the lack of interface connectivity and electrical conductivity between particles.[24,25] Moreover, dissolution of polysulfide compounds is inevitable because the nonpolar carbon material has only a weak physical restriction on the polar polysulfide.[26,27] Furthermore, the slow redox kinetics of polysulfide hinders the rapid and complete conversion between soluble polysulfides and Li_2S_2/Li_2S, which is also an important factor restricting the performance of lithium–sulfur batteries.[28–31]

Here, we report the preparation of a three-dimensional porous carbon (TDPC) with larger pore volume and electrochemical catalytic activity. Encapsulated sulfur particles in

---

[a] Guangxi University of Science and Technology, Guangxi Key Laboratory of Automobile Components and Vehicle Technology, Liuzhou 545006, China. E-mail: lxh304@aliyun.com

[b] China School of Automotive and Transportation Engineering, Guangdong Polytechnic Normal University, Guangzhou, 510632, China. E-mail: zsbqiche@163.com

† Electronic supplementary information (ESI) available. See DOI: 10.1039/d1ra02704b

TDPC were synthesized through a removable hard-template method (Fig. 1a). Our electrochemical experiments verified the advantages of TDPC as the sulfur host. Firstly, the abundant uniform mesopores in TDPC enabled high sulfur content (68 wt%), and the high ion conductivity allowed fast ion transfer during the discharge–charge reactions. Secondly, the Co nanoparticles and N-doped carbon composite in TDPC enhanced the catalytic effect, which improved the conversion kinetics between liquid-state Li_2S_6 and solid-state Li_2S. Consequently, the fabricated TDPC@S electrodes were tested for good electrochemistry and featured a high discharge specific capacity of 912.8 mA h g^{-1} at 1C and a low fading rate of 0.0937% per cycle for 500 cycles.

Results and discussion

The TDPC@S composite was prepared by the removable template approach illustrated in Fig. 1a. Cobalt nitrate and imidazole ligands were successively mixed with silica nanospheres. A large number of deposition sites were formed on the surface of modified nanospheres, which would be beneficial for the uniform deposition of ZIF-67 in the interspace of silicon nanospheres. In the next steps, a high-temperature carbonization process allowed the production of interconnected carbon skeleton embedded between the silica nanospheres. After template removal by chemical etching, the previous three-dimensional (3D) carbon matrix was not destroyed, maintaining the interconnected mesoporous structure. Then, sulfur element was infused into the structural pores of TDPC to form the TDPC/S composites by a facile melt-diffusion process. Finally, we heated the TDPC/S materials with nitrogen purging to remove the uncoated sulfur particles. This design of TDPC@S exhibits three outstanding beneficial features for the Li–S battery cathode. (i) The robust 3D architecture of TDPC with large surface area and high porosity encapsulates more sulfur, resulting in a higher active material content and providing faster electron transfer and ion diffusion paths; (ii) the TDPC enables spatially controlled deposition of Li_2S nanoparticles on the inner surface of the TDPC shell, which effectively prevents the diffusion of soluble polysulfides by physisorption between TDPC and polysulfides; (iii) importantly, the Co nanoparticles and N-doped carbon composite in TDPC function as electrocatalytic sites to accelerate the reversible conversion between high-order lithium polysulfide (Li_2S_8) and low-order lithium polysulfide (Li_2S; Fig. 1b). Benefiting from the aforementioned advantages, the TDPC@S cathodes display a good cycling performance up to 500 cycles.

The morphologies and structures of the materials were characterized and analysed by scanning electron microscopy (SEM) combined with energy-dispersive spectrometry (EDS) and transmission electron microscopy (TEM) with elemental mapping. It can be observed that the granuliform SiO_2 templates are isolated nanoparticles with a uniform grain size of approximately 400 nm (Fig. 2a). After coating of the packed SiO_2 by ZIF, the spherical SiO_2 becomes larger and has a dense structure, as shown in Fig. 2b. The EDS clearly reveals the silicon and oxygen element distribution on the ZIF-coated spherical SiO_2 (Fig. S1†). As a comparison, there was no silicon element energy spectrum in the EDS spectra after the template was removed, indicating that the SiO_2 template has been completely removed by subsequent processes (Fig. S2).† Fig. S3† shows the SEM image of ZIF-coated spherical SiO_2 material after carbonization. It is noted that structure of the spherical SiO_2 template is not damaged by high temperature. Then, the SiO_2 templates were removed by chemical etching technique using KOH as etchant. Fig. 2c shows the SEM image of the obtained TDPC, which presents a good hollow three-dimensional structure. Further study by TEM investigation shows a large number of pore structures inside the TDPC (Fig. 2d). This porous structure can be loaded with more active sulfur, which is conducive to the preparation of high energy density Li–S batteries. At the same time, the high-resolution TEM images also unveil the existence of a mass of cobalt nanoparticles implanted in the TDPC matrix (Fig. 2e and f). To further reveal the elemental distribution within the TDPC matrix, the elemental mappings in overall view and of carbon,

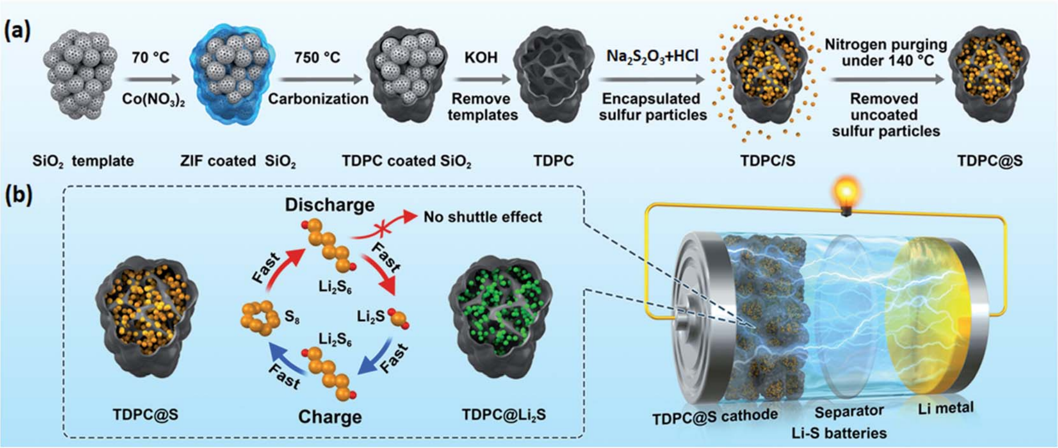

Fig. 1 (a) Schematic of the synthetic process for TDPC@S materials, (b) schematic illustration of the effects of TDPC in improving the conversion kinetics between the solid-state polysulfides (Li_2S_2, Li_2S) and liquid-state polysulfides (Li_2S_8, Li_2S_6, Li_2S_4).

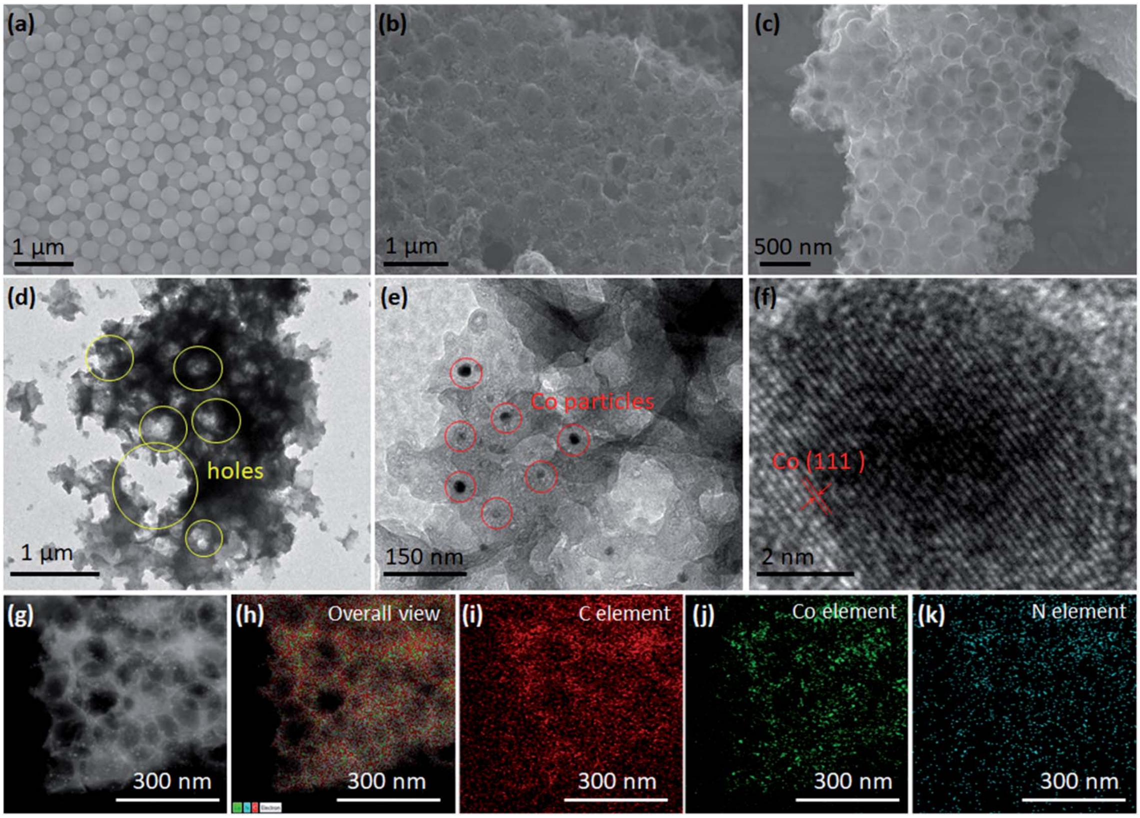

Fig. 2 SEM images of (a) SiO_2 spherical template, (b) ZIF-coated spherical SiO_2, and (c) TDPC. (d–f) TEM images of TDPC. (g) SEM image of TDPC and corresponding elemental maps: (h) overall view, (i) C element, (j) Co element, and (k) N element.

cobalt, and nitrogen were performed and are shown in Fig. 2g, demonstrating that there are a large number of holes in the TDPC, and the abovementioned elements are homogenously distributed in the TDPC matrix (Fig. 2h–k). After sulfur impregnation, the obtained TDPC@S maintained the three-dimensional structure (Fig. S4a†). From the elemental mappings shown in Fig. S4b–f,† we clearly observed that the sulfur and cobalt particles are homogenously implanted on the three-dimensional carbon walls.

As shown in the nitrogen adsorption–desorption isotherm of the as-prepared TDPC in Fig. 3a, the curves are a type II isotherm associated with an H3 hysteresis loop. The Brunauer–Emmett–Teller (BET) surface area and total pore volume of the TDPC sample are 426.2 $m^2\ g^{-1}$ and 0.85 $cm^3\ g^{-1}$, respectively, which are higher than those of the TDPC@S sample (43.2 $m^2\ g^{-1}$, 0.23 $cm^3\ g^{-1}$) because of the introduction of pure sulfur with a smaller pore volume (12.6 $m^2\ g^{-1}$, 0.16 $cm^3\ g^{-1}$). The corresponding pore size distributions suggest that the three aforementioned samples have hierarchically distributed pores of different sizes, including micropores and mesopores. For quantitative analysis of sulfur content in the TDPC@S sample, thermogravimetric (TG) measurement was performed. From Fig. 3c, the TDPC sample exhibited only a minimal weight loss at the temperature range of 30 °C to 800 °C when it was treated at 800 °C. Meanwhile, the pure sulfur is entirely lost in the temperature range of 150 °C to 300 °C because of sublimation. Thus, it is confirmed that the sulfur content is 68.65% in the TDPC@S composite. X-ray diffraction (XRD) spectrums of the three composites are shown in Fig. 3d. No obvious peaks of SiO_2 are observed in the TDPC material, which suggests the SiO_2 template has been completely removed. The XRD spectrum of the TDPC@S shows peaks of both TDPC (36.93°) and pure sulfur (23.08°), indicating the presence of both components. The amorphous states of TDPC and TDPC@S were measured by Raman spectroscopy, as shown in Fig. 3e. The intensity ratios between the D band and G band for TDPC and TDPC@S are 1.03 and 1.02, respectively. The above results indicate that introduction of sulfur particles in TDPC did not change the degree of graphitization. An experiment on adsorption of polysulfide lithium was carried out using TDPC, as shown in Fig. 3f. It is obvious that the solution becomes clarified with the addition of TDPC. This phenomenon shows that TDPC has a good adsorption effect for polysulfide lithium. UV-vis spectroscopy defines the liquid intermediates in the discharging process.[32,33] We investigated the UV-vis spectra to demonstrate the adsorption of TDPC on lithium polysulfide. The UV-vis spectrum shows the absorption peak at *ca.* 418 nm for S_4^{2-} (Fig. S5†), which has been reported in previous literature.[34,35] The UV-vis spectrum of solution 4 showed that the absorption peak intensity of S_4^{2-} was weakened after the addition of TDPC. The evidence above also indicates the adsorption of polysulfide lithium using TDPC. To further investigate the chemical status

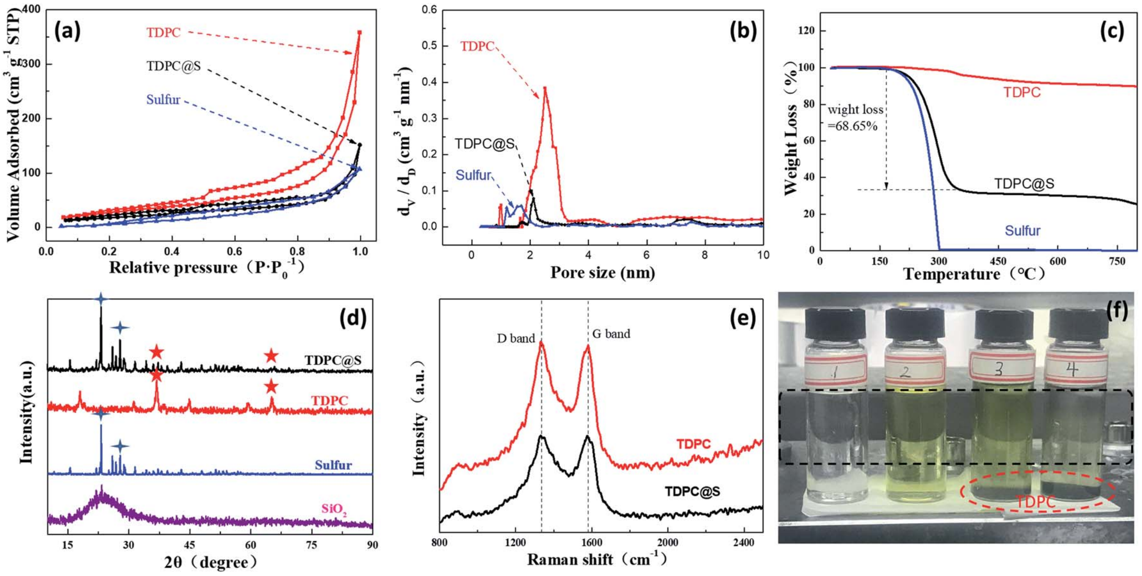

Fig. 3 (a) Nitrogen desorption curves of as-prepared TDPC, TDPC@S, and pure sulfur; (b) aperture distribution curves of as-prepared TDPC, TDPC@S, and pure sulfur; (c) TGA curves of as-prepared TDPC, TDPC@S, and pure sulfur under an inert atmosphere; (d) XRD patterns of as-prepared TDPC, TDPC@S, pure sulfur, and spherical SiO_2; (e) Raman spectra of as-prepared TDPC and TDPC@S; (f) digital photographs of different solutions before and after the addition of various compounds: solution 1, pure electrolyte; solution 2, Li_2S added into pure electrolyte; solution 3, TDPC added into solution 2; solution 4, after leaving solution 3 for 30 minutes.

of carbon, nitrogen, and cobalt elements in the TDPC@S, the full spectrum and high-resolution C 1s, N 1s, and Co 2p spectrums of the TDPC@S sample were illuminated by X-ray photoelectron spectroscopy (XPS). As shown in Fig. 4a, six normal peaks located at 164.43, 227.51, 286.29, 399.37, 533.74, and 799.08 eV were found, which correspond to the binding energy of S 2p, S 2s, C 1s, N 1s, O 1s, and Co 2p.[36,37] The surface composition of the elements mentioned above is estimated to be 9.5% for sulfur, 55.7% for carbon, 8.3% for nitrogen, 21.2% for oxygen, and 5.3% for cobalt. From Fig. 4b, the high-

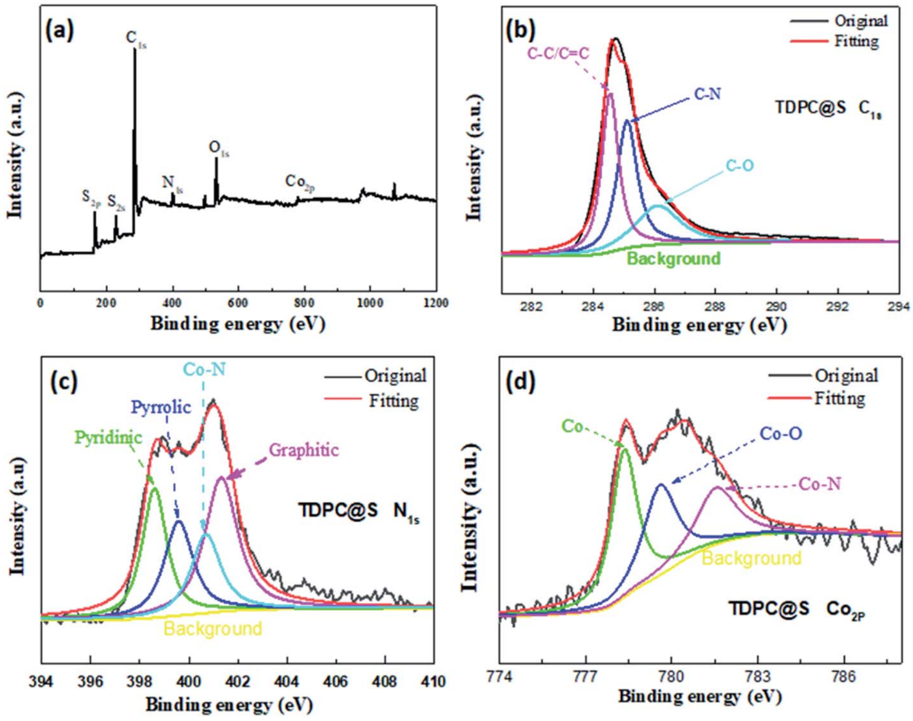

Fig. 4 High-resolution XPS spectra of TDPC: (a) full spectrum, (b) C 1s, (c) N 1s, (d) Co 2p.

resolution C 1s spectrum can be further convoluted into C–C/C═C (284.6 eV), C–N (285.2 eV), and C–O (286.2 eV).[38] The high-resolution N 1s spectrum is deconvoluted into four peaks of different signals with binding energies of 398.6, 399.5, 400.6, and 401.3 eV, which are indexed to pyridinic N, pyrrolic N, Co–N, and graphitic N, respectively.[39] Peaks at 778.3, 779.6, and 781.5 eV are assigned to metallic Co, Co–O, and Co–N, respectively, which attest to the existence of Co–N bonding.[40] Many reports show that the introduction of Co–N bonding and pyridinic-N are beneficial for improving polysulfide redox kinetics.[41,42] In the sulfur reduction process, these abundant pyridinic-N and cobalt–nitrogen active sites, as matrix catalyst, accelerate the conversion of lithium polysulfide, leading to enhanced electrode stability.[43]

The prepared electrode was assembled into a CR2032-type button cell to evaluate the electrochemical performance of TDPC@S as cathode. The TDPC/S cathode and the mixture of sulfur and acetylene black (S/C) cathode were also made into CR2032-type button cells for comparison. Fig. 5a presents the representative electrochemical impedance spectroscopy (EIS) profiles of the batteries with the three aforementioned cathodes at a frequency range of 10^{-2}–10^{5} Hz. According to the equivalent circuit diagram (Fig. S6†), the fitting results show that the TDPC@S electrode has a much smaller R_{ct} than the other two electrodes, indicating that TDPC can effectively facilitate charge transfer and improve the polysulfide redox reactions. To investigate the effects of TDPC on the stability of the electrode, cyclic voltammetry (CV) tests were conducted, as shown in Fig. 5b. The CV profiles display two sulfur reduction peaks, which locate at 2.31 V and 2.03 V in the negative scan, corresponding to the two discharge platforms in Fig. 5d. The fifth CV profile coincides with the first CV profile, verifying that the electrode has good stability. To further evaluate the cycling stability of the Li–S batteries based on TDPC cathode, charge–discharge test was conducted at 0.25C for 100 cycles with a sulfur loading of 3.8 mg cm^{-2} (Fig. 5c). As shown in Fig. 5d and S7,† the discharge specific capacity of the TDPC@S cathode is 964.36 mA h g^{-1} at the first cycling. After 100 charge–discharge cycles, the capacity of the electrode dropped to 700.75 mA h g^{-1}, corresponding to a 72.61% capacity retention rate. These values are 60.06% for the TDPC/S cathode and 23.6% for S/C cathode. The potential gap (ΔU) is an important index to evaluate the charge efficiency.[44] The ΔU of the TDPC@S electrode is obviously smaller after 100 charge–discharge cycles than that of the other two electrodes, indicating the TDPC@S electrode has a relatively low resistance and polarization. Fig. 5e and f show the rate performance of the three electrodes, which were evaluated at various current densities (from 0.1C to 2C). The discharge specific capacities of the TDPC@S electrode are 1139.2 mA h g^{-1}, 959.9 mA h g^{-1}, 813.5 mA h g^{-1}, 519.6 mA h g^{-1} and 349.1 mA h g^{-1} at 0.1, 0.25, 0.5, 1 and 2C, respectively. Those values are 1023.6 mA h g^{-1}, 841.5 mA h g^{-1}, 718.1 mA h g^{-1}, 336.6 mA h g^{-1}, and 151.9 mA h g^{-1} for the TDPC/S cathode (Fig. S8a†), and 757.8 mA h g^{-1}, 616.0 mA h g^{-1}, 433.1 mA h g^{-1}, 272.1 mA h g^{-1}, and 119.2 mA h g^{-1} for the S/C cathode (Fig. S8b†) at the relevant rates. More importantly, compared with the other two cathodes, the reversible capacity of the TDPC@S cathode was basically recovered, with the current density back to 0.1C. Such phenomena further prove the TDPC@S cathode has enhanced reaction kinetics.

The long-term cycling performance of the three cathodes was tested at a high rate current density of 1C, as shown in Fig. 6. Compared with the other two cathodes, the cycling curve of the TDPC@S cathode exhibits better cycle stability, with the capacity retention of 62.58% after 500 cycles, corresponding to

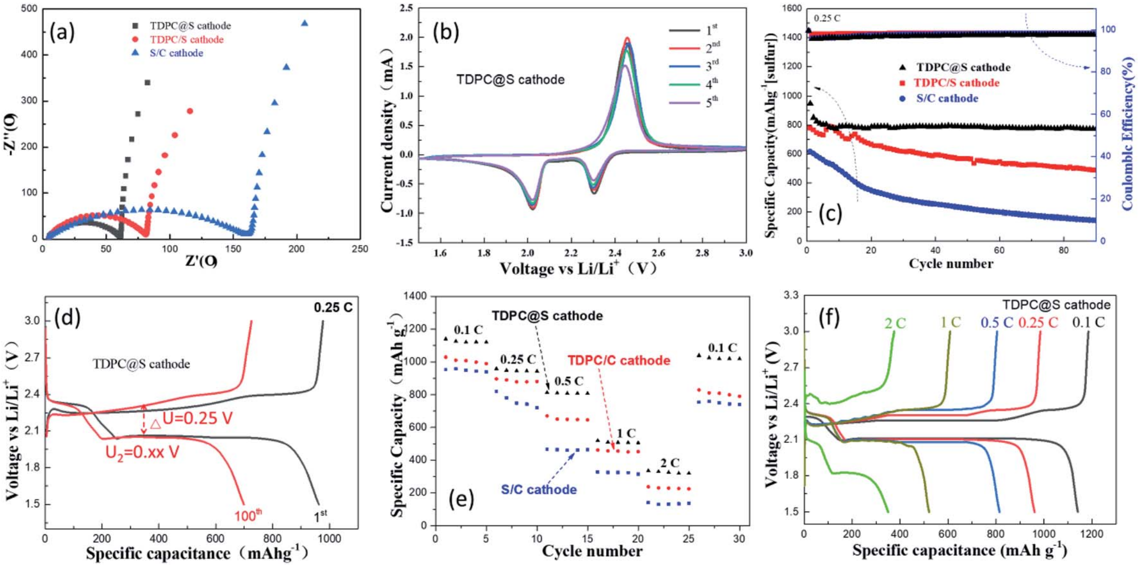

Fig. 5 (a) EIS curves of TDPC@S cathode, TDPC/S cathode, and S/C cathode; (b) CV curves of TDPC@S cathode; (c) cycling performance with coulombic efficiency of the TDPC@S, TDPC/S, and S/C cathodes at 0.2C for 100 cycles; (d) charge and discharge curves of the first cycle and the hundredth cycle of the TDPC@S cathode at 0.25C; (e) cyclic stability of the TDPC@S, TDPC/S, and S/C cathodes at different current densities; (f) charge–discharge curves of the TDPC@S cathode at different current densities.

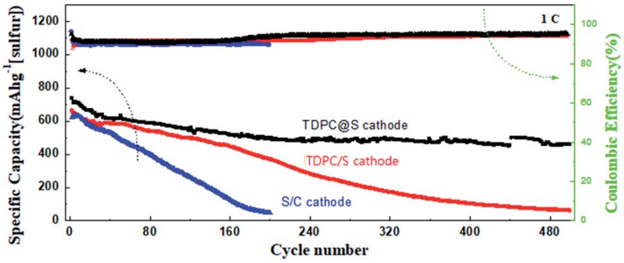

Fig. 6 Cycling performance of TDPC@S, mixture of sulfur and TDPC, and S/C cathodes at 1C over 500 cycles.

a capacity decay of only 0.0937% per cycle. These values are 0.476% for the TDPC/C cathode and 1.285% for the S/C cathode. These results further validated that the TDPC@S cathode has better cycle stability than the other two cathodes. Table S1† summarizes the performance of sulfur-based cathodes for Li–S batteries in the published literature. Note that the performance of the TDPC@S cathode is better than (or at least comparable to) the leading results reported for other cathodes (Table S1†).

Experimental

Synthesis of TDPC and TDPC@S samples

TDPC was synthesized by adopting a procedure based on a removable-template approach.[45] In a typical synthesis, 15 mL of deionized water was mixed with 55 mL ethyl alcohol under magnetic stirring. Then, 3 mL of tetraethyl orthosilicate and 4 mL of ammonia were poured into the above solution, respectively. After magnetic stirring for 5 hours, the precipitate was collected by centrifugation at 4000 rpm and washed with deionized water three times. Dry nano-SiO_2 particles were obtained after 60 °C heat treatment for 12 hours. Next, 0.873 g of cobalt nitrate hexahydrate was dissolved in 10 mL of anhydrous methanol. The obtained 1.0 g of nano-SiO_2 particles were then added into the above solution. After stirring, ultrasonic treatment, and drying, we collected the pink powder. Next, 0.985 g of 2-methylimidazole was dissolved in 10 mL anhydrous methanol, and 1.5 g of the pink powder was added into the anhydrous methanol solution under magnetic stirring. Purple ZIF67@SiO_2 composites were obtained after 70 °C heat treatment for 1 hour. Then, we heated the ZIF67@SiO_2 composites at 750 °C for 3 hours, and the cooled powder was soaked in KOH (3 M) solution for 8 hours to remove the SiO_2 template. Through the above steps, we obtained the TDPC sample.

For TDPC@S, firstly, 12.1 g of sodium thiosulfate was dissolved in a mixture of water and ethanol (v/v = 25 mL : 25 mL) under magnetic stirring. Then, 0.3 g of the prepared TDPC was slowly added into the solution. Secondly, 5 mL of diluted hydrochloric acid was added into the solution to form sulfur nanoparticles. We collected the mixture of TDPC and sulfur (TDPC/C) by centrifugation at 8000 rpm for 20 minutes. Lastly, the TDPC@S was obtained after heating at 140 °C for 20 minutes under 200 mL min^{-1} nitrogen gas flow, which removed the sulfur particles outside the TDPC.

Materials characterization

The surface morphologies and structures of the prepared samples were analyzed by scanning electron microscopy (SEM) along with energy-dispersive X-ray spectroscopy (Hitachi S-4800), transmission electron microscopy (TEM along with elemental mapping, G2 F20FEI Tecnai G2 F20), and X-ray photoelectron spectroscopy (XPS, PHI). The sulfur content was tested by thermogravimetric analysis (TGA, METTLER) under a N_2 atmosphere at a temperature ramp rate of 10 °C min^{-1}. Pore-size distributions and adsorption–desorption isotherms were carried out with a Quadrasorb SIMP apparatus. Raman spectra were performed using an instrument (HORIBA) with an Ar laser source of 633 nm.

Electrode and coin-battery assembly

Firstly, 0.02 g of polyvinylidene fluoride (PVDF) was completely dissolved in 2 mL of *N*-methyl pyrrolidone (NMP). Then, 0.16 g of TDPC@S and 0.2 g of conductive carbon (Super P) were added into the solution to form a uniform slurry. The obtained slurry was cast on the surface of an aluminum film with a thickness of 300 μm. Then, the aluminum film was cut into small round pieces of 12 mm (thickness 0.3 mm, *ca.* 3.1 mg per disk) in diameter after the slurry was dried. Lastly, coin-type cells (CR 2032) were assembled with TDPC@S as the cathode, a lithium foil (12 mm in diameter, 0.3 mm in thickness) as the anode, Celgard 2400 (14 mm; *ca.* 1.2 mg per piece) as a diaphragm, and 1.0 mol L^{-1} lithium bis(trifluoromethanesulfonyl)imide (LiTFSI) with 0.1 mol L^{-1} of $LiNO_3$ in 1,3-dioxolane and 1,2-dimethoxyethane (v/v = 1 : 1) as the electrolyte (*ca.* 13 mg per cell). According to weight and calculation, the sulfur mass loading is around 3.8 mg cm^{-2}.

Electrochemical measurements

The charge–discharge measurements were tested using a CT2001A cell test instrument (Wuhan LAND Electronic Co, Ltd 20 mA). The cyclic voltammetry (CV) and electrochemical impedance spectroscopy (EIS) measurements were conducted with a CHI660E (Shanghai CH Instrument Co, Ltd) electrochemical workstation.

Conclusions

In summary, we have successfully synthesized TDPC with a larger pore volume and electrochemical catalytic activity as a new sulfur host for Li–S batteries. With the advantages mentioned above, the TDPC@S composite is loaded with the sulfur content of 68.65% and a high areal mass sulfur loading of 3.8 mg cm^{-2}. Compared with the two other types of cathode, The Li–S batteries with the TDPC@S cathode deliver higher rate capacities and reversible cycling capacities.

Conflicts of interest

There are no conflicts to declare.

Acknowledgements

This work was supported by the Fund Project of the GDAS Special Project of Science and Technology Development, Guangdong Academy of Sciences Program (No. 2020GDASYL-20200104030); the Innovation Project of Guangxi University of Science and Technology Graduate Education (YCSW2020217); Guangxi Innovation Driven Development Project (No. AA18242036-2); the Fund Project of the Key Lab of Guangdong for Modern Surface Engineering Technology (No. 2018KFKT01); and the Science and Technology Planning Projects of Guangzhou (No. 201803030041).

Notes and references

1 X. L. Xing, H. B. Dong, S. Y. Zhang, Y. Li, L. X. Liu, D. X. Yu, Y. F. Sheng, C. Y. Yi and G. Han, *Energy Storage Sci. Technol.*, 2020, **9**, 239–248.
2 A. Manthiram, X. W. Yu and S. F. Wang, *Nat. Rev. Mater.*, 2017, **2**, 16103.
3 M. J. Mühlbauer, O. Dolotko, M. Hofmann, H. Ehrenberg and A. Senyshyn, *J. Power Sources*, 2017, **348**, 145–149.
4 M. Liu, N. P. Deng, J. G. Ju, L. L. Fan, L. Y. Wang, Z. J. Li, H. J. Zhao, G. Yang, W. M. Kang, J. Yang and B. W. Chen, *Adv. Funct. Mater.*, 2019, **29**, 1905467.
5 J. H. Kim, Y. H. Lee, S. J. Cho, J. G. Gwon, H. J. Cho, M. Jang and S. Y. Lee, *Energy Environ. Sci.*, 2019, **12**, 177.
6 T. Kim, W. T. Song, D. Y. Son, L. K. Ono and Y. B. Qi, *J. Mater. Chem. A*, 2019, **7**, 2942–2964.
7 Y. Z. Song, W. L. Cai, L. Kong, J. S. Cai, Q. Zhang and J. Y. Sun, *Adv. Energy Mater.*, 2019, 1901075.
8 H. Wang, W. Zhang, H. Liu and Z. Guo, *Angew. Chem., Int. Ed.*, 2016, **55**, 3992–3996.
9 R. Mo, D. Rooney, K. Sun and H. Y. Yang, *Nat. Commun.*, 2017, **8**, 13949.
10 K. Chen, Z. Sun, R. Fang, Y. Shi, H. M. Cheng and F. Li, *Adv. Funct. Mater.*, 2018, **28**, 1707592.
11 Y. Li, J. Fan, J. Zhang, J. Yang, R. Yuan, J. Chang, M. Zheng and Q. Dong, *ACS Nano*, 2017, **11**, 11417–11424.
12 K. L. Zhu, C. Wang, Z. X. Chi, F. Ke, Y. Yang, A. B. Wang, W. K. Wang and L. X. Miao, *Front. Energy Res.*, 2019, **7**, 123.
13 X. Gao, Q. Sun, X. Yang, J. Liang, A. Koo, W. Li, J. Liang, J. Wang, R. Li, F. B. Holness, A. D. Price, S. Yang, T. K. Sham and X. Sun, *Nano Energy*, 2019, **56**, 595–603.
14 S. Y. Lang, R. J. Xiao, L. Gu, Y. G. Guo, R. Wen and L. J. Wan, *J. Am. Chem. Soc.*, 2018, **140**, 8147–8155.
15 D. H. Liu, C. Zhang, G. M. Zhou, W. Lv, G. W. Ling, L. J. Zhi and Q. H. Yang, *Adv. Sci.*, 2018, **5**, 1700270.
16 X. J. Liu, T. Qian, J. Liu, J. H. Tian, L. Zhang and C. L. Yan, *Small*, 2018, **14**, 1801536.
17 S. Suriyakumar, S. Gopi, M. Kathiresan, S. Bose, E. B. Gowd, J. R. Nair, N. Angulakshmi, G. Meligrana, F. Bella and C. Gerbaldi, *Electrochim. Acta*, 2018, **285**, 355–364.
18 X. J. Yu, G. M. Zhou and Y. Cui, *ACS Appl. Mater. Interfaces*, 2019, **11**, 3080–3086.
19 Y. Xie, G. Y. Pan, Q. Jin, X. Q. Qi, T. Wang, W. Li, H. Xu, Y. H. Zheng, S. Li, L. Qie, Y. H. Huang and J. Li, *Adv. Sci.*, 2020, **7**(9), 1903168.
20 Z. W. She, W. Y. Li, J. J. Cha, G. Y. Zheng, Y. Yang, M. T. McDowell, P. C. Hsu and Y. Cui, *Nat. Commun.*, 2013, **4**, 1331–1336.
21 H. Kim, J. Lee, H. Ahn, O. Kim and M. J. Park, *Nat. Commun.*, 2015, **6**, 7278–7286.
22 K. Park, J. H. Cho, J. H. Jang, B. C. Yu, A. T. De, L. Hoz, K. M. Miller, C. J. Ellison and J. B. Goodenough, *Energy Environ. Sci.*, 2015, **8**, 2389.
23 J. Zhang, C. P. Yang, Y. X. Yin, L. J. Wan and Y. G. Guo, *Adv. Mater.*, 2016, **28**, 9539–9544.
24 Q. Pang, X. Liang, C. Y. Kwok and L. F. Nazar, *Nat. Energy*, 2016, **1**, 16132.
25 M. Agostini and A. Matic, *Small*, 2019, **1**, 1905585.
26 S. B. Zeng, L. G. Li, L. H. Xie, D. K. Zhao, N. Wang and S. W. Chen, *ChemSusChem*, 2017, **10**, 3378–3386.
27 J. Xie, B. Q. Li, H. J. Peng, Y. W. Song, M. Zhao, X. Chen, Q. Zhang and J. Q. Huang, *Adv. Mater.*, 2019, **31**, 1903813.
28 C. Zhao, G. L. Xu, T. S. Zhao and K. Amine, *Angew. Chem., Int. Ed.*, 2020, **59**(40), 17634–17640.
29 M. Zhao, H. J. Peng, B. Q. Li, X. Chen, J. Xie, X. Y. Liu, Q. Zhang and J. Q. Huang, *Angew. Chem., Int. Ed.*, 2020, **59**, 9011–9017.
30 B. Q. Li, L. Kong, C. X. Zhao, Q. Jin, X. Chen, H. J. Peng, J. L. Qin, J. X. Chen, H. Yuan, Q. Zhang and J. Q. Huang, *Infomat*, 2019, **1**(4), 533–541.
31 M. Zhao, B. Q. Li, X. Chen, J. Xie, H. Yuan and J. Q. Huang, *Chem*, 2020, **6**(12), 3297–3311.
32 C. Barchasz, F. Molton, C. Duboc, J.-C. Lepretre, S. Patoux and F. Alloin, *Anal. Chem.*, 2012, **84**, 3973–3980.
33 Q. He, A. T. S. Freiberg, M. U. M. Patel, S. Qian and H. A. Gasteiger, *J. Electrochem. Soc.*, 2020, **167**, 080508.
34 H. L. Wu, M. Shin, Y. M. Liu, K. A. See and A. A. Gewirth, *Nano energy*, 2017, **32**, 50–58.
35 N. A. Cañas, D. N. Fronczek, N. Wagner, A. Latz and K. A. Friedrich, *J. Phys. Chem. C*, 2014, **118**, 12106–12114.
36 X. Peng, K. Huo, J. Fu, X. Zhang, B. Gao and P. K. Chu, *Chem. Commun.*, 2013, **49**, 10172–10174.
37 G. Vardar, W. J. Bowman, Q. Y. Lu, J. Y. Wang, R. J. Chater, A. Aguadero, R. Seibert, J. Terry, A. Hunt, I. Waluyo, D. D. Fong, A. Jarry, E. J. Crumlin, S. L. Hellstrom, Y. M. Chiang and B. Yildiz, *Chem. Mater.*, 2018, **30**(18), 6259–6276.
38 C. Zu and A. Manthiram, *Adv. Energy Mater.*, 2013, **3**, 1008–1012.
39 C. O. Baker, X. Huang, W. Nelson and R. B. Kaner, *Chem. Soc. Rev.*, 2017, **46**, 1510–1525.
40 X. R. Wang, J. Y. Liu, Z. W. Liu, W. C. Wang, J. Luo, X. P. Han, X. W. Du, S. Z. Qiao and J. Yang, *Adv. Mater.*, 2018, **30**, 1800005.
41 Y. J. Li, J. B. Wu, B. Zhang, W. Y. Wang, G. Q. Zhang, Z. W. Seh, N. Zhang, J. Sun, L. Huang, J. J. Jiang, J. Zhou and Y. M. Sun, *Energy Storage Mater.*, 2020, **30**, 250–259.

42 Q. C. Li, Y. Z. Song, R. Z. Xu, L. Zhang, J. Gao, Z. Xia, Z. N. Tian, N. Wei, M. H. Rümmeli, X. L. Zou, J. Y. Sun and Z. F. Liu, *ACS Nano*, 2018, **12**, 10240–10250.

43 R. Wang, J. L. Yang, X. Chen, Y. Zhao, W. G. Zhao, G. Y. Qian, S. N. Li, Y. G. Xiao, H. Chen, Y. S. Ye, G. M. Zhou and F. Pan, *Adv. Energy Mater.*, 2020, **10**, 1903550.

44 A. Eftekhari, *Sustainable Energy Fuels*, 2017, **1**, 2053.

45 A. I. Douka, Y. Y. Xu, H. Yang, S. Zaman, Y. Yan, H. F. Liu, M. A. Salam and B. Y. Xia, *Adv. Mater.*, 2020, 2002170.